Development of a voltage-behavior model for NiMH batteries using an impedance-based modeling concept

Marc Thele [a],*, Oliver Bohlen [a], Dirk Uwe Sauer [a], Eckhard Karden [b]

[a] *Institute for Power Electronics and Electrical Drives ISEA, RWTH Aachen University, Jaegerstr. 17/19, 52066 Aachen, Germany* [1]
[b] *Ford Research Center Aachen, Suesterfeldstrasse 200, 52079 Aachen, Germany*

Abstract

To handle the complexity of modern automotive power nets, simulation-based design methods are important and suitable models of all system components including the battery as a main part are therefore mandatory. However, simulation models of energy storage devices are difficult to obtain. In particular, batteries are time-variant and strongly non-linear. An impedance-based modeling approach has been applied that copes with these characteristics and offers the development and parameterization of powerful models covering a wide dynamic range. As an example, this paper outlines the development of a NiMH battery model. Besides the impedance-based part of the model, the influences of the typical hysteresis effect of NiMH batteries is described in detail and an empirical modeling approach is introduced. The presented model is already successfully used by an automotive manufacturer which reflects the applicability of the modeling approach.
© 2007 Elsevier B.V. All rights reserved.

Keywords: NiMH battery; Hysteresis; Battery model; Simulation; Impedance spectroscopy

1. Introduction

As a successful example for impedance-based modeling and as an interesting application for hybrid electric vehicles, this paper introduces the development of a NiMH battery model. A non-linear impedance-based model core (see Section 2) is extended by a model part which considers the typical hysteresis phenomenon of NiMH batteries (Section 3). This part of the model is parameterized in the time domain and allows together with the impedance-based model core for a large validity range. The synergies when combining impedance-based modeling approaches and time-domain based model parts become observable.

The impedance-based modeling approach employs electrochemical impedance spectroscopy (EIS) [1]. The measurements were carried out with the EISmeter, an impedance spectroscope that operates in galvanostatic mode and has been developed especially for batteries and fuel cells at our institute [2]. Small-signal

excitations (I_{ac}) and the evaluation of the system's response enable accurate investigations at nearly any working point (state of charge, temperature, dc-current). The models are built by joining universal electrical components such as inductors, capacitors and (non-linear) resistors. Physico-chemical processes can easily and effectively be modeled this way providing also a minimized computation effort. The method is applicable for all kinds of electrochemical energy storage devices [3] and [4].

A similar modeling approach is given in [5] for a NiMH battery, however, without considering non-linear resistances and without modeling the typical hysteresis phenomenon which significantly influences the NiMH equilibrium-potential. Unlike other battery technologies, the equilibrium potential of NiMH batteries is not unambiguously determined by the state of charge (SOC) due to this phenomenon [6] and [7]. Consequently, an empirical hysteresis model has been developed for the prediction of the equilibrium potential and is combined with the impedance-based model which determines the dynamic overvoltages during current flows.

The complete model implementation and a general overview on how to parameterize the models are given in this paper. The modeling approach is evaluated by comparing the measured and the simulated battery voltage corresponding to several current

* Corresponding author. Tel.: +49 241 80 969 45; fax: +49 241 80 922 03.
E-mail address: marc.thele@gmx.de (M. Thele).
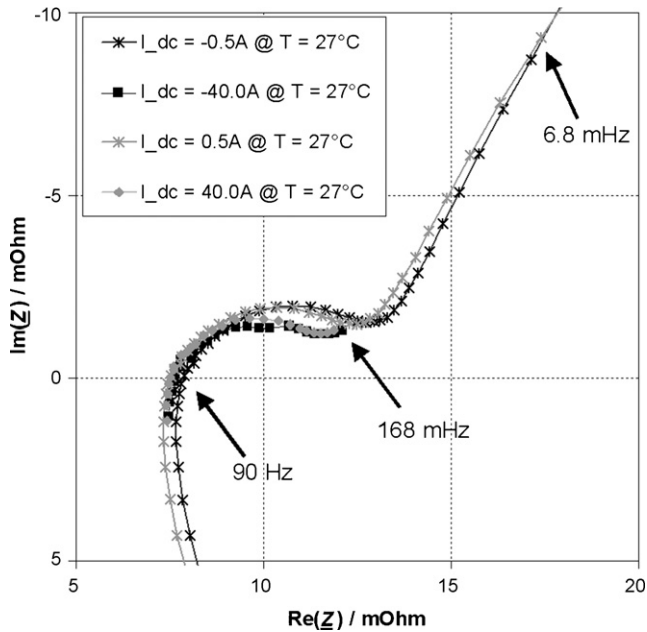[1] batteries@isea.rwth-aachen.de.

Fig. 1. Impedance spectra with different superimposed direct currents I_{dc} of a NiMH battery at 70% SOC and 27 °C (battery type: Sanyo Hr-DP, 6.5 Ah).

profiles with different dynamics and current rates. All investigations have been performed on cylindrical battery samples produced by Sanyo ("Hr-DP") and Panasonic ("HHR 650 D"), both rated with a nominal capacity C_N of 6.5 Ah.

2. The impedance-based core of the battery model

Impedance spectra (Fig. 1) were obtained by applying an ac signal (I_{ac}) with different defined frequencies and evaluating the system's responses. After the measurement of each frequency, the amplitude of the ac voltage signal was automatically evaluated during the measurement. For the next signal frequency to be investigated, the amplitude of the ac current signal was adapted to keep the voltage amplitude smaller than a definable value. Thus, the non-linearity of the battery is considered. Limited amplitudes of approximately 3 mV per cell are usable [1]. For accurate investigations at different working points, bias currents (I_{dc}) were applied and specific cell temperatures and SOCs were set for the measurement of each spectrum. The temperature and the SOC were kept fixed as accurately as possible during the measurement since the impedance is a function of both states. To assure comparable conditions at the beginning and at the end of the measurement of one impedance spectrum, the maximum change of the state of charge during this time was limited to $\Delta SOC < 5\%$.

The following characteristics can be identified by the evaluation of the NiMH impedance spectra (Fig. 1). The spectra show an inductive behavior (L) at high frequencies which is mainly caused by the metallic connectors of the battery. The pure ohmic resistance (R_i) can be detected by the minimum of the real part of the impedance spectra (at about 90 Hz). R_i reflects the limited conductance of the contacts, the active masses and the electrolyte. The semicircle is caused by charge-transfer processes

and charged double layers inside the battery. The changing diameter indicates the non-linearity of the charge-transfer processes. Different direct current rates I_{dc} have been superimposed to the small signal excitations I_{ac} to investigate this behavior. More detailed information on this measurement procedure can be found in Refs. [3] and [4].

The semicircle can be modeled by a parallel connection of a non-linear resistor R_{ct} and a capacitor C_{dl}. At lower measurement frequencies ($f < 168$ mHz), the diffusion behavior of the battery becomes apparent which is commonly modeled by a so-called Warburg impedance Z_w. Based on this data, an equivalent electrical circuit of a NiMH battery can be developed (Fig. 2) and, additionally, be parameterized.

Particular attention has to be paid to the non-linear behavior of the charge-transfer resistance R_{ct} of batteries. Generally, this behavior can be described by the so-called Butler–Volmer equation with I_0 as the exchange current, n as the number of transferred elementary charges, η as the overpotential, α as a symmetry coefficient, T as the absolute temperature and k as the Boltzmann constant ($8.617 \times 10E-5$ eV K^{-1}):
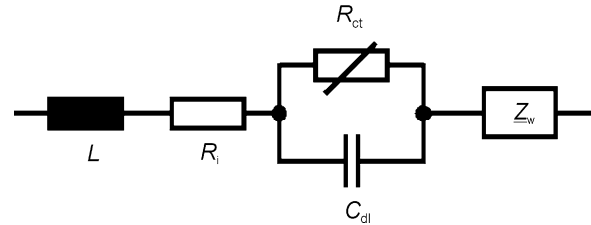

Fig. 2. Equivalent electrical circuit diagram of a NiMH battery representing the overpotential during charging and discharging without modeling of the equilibrium potential.

$$I = I_0 \left(\exp\left(\frac{n\alpha\eta}{kT}\right) - \exp\left(\frac{-n(1-\alpha)\eta}{kT}\right) \right) \qquad (1)$$

A charge-transfer characteristic can also be observed for NiMH batteries. Fig. 3 exemplarily illustrates the current dependent values for R_{ct} (with $R_{ct} = (d\eta/dI)$) at 27 °C and 70% state of charge (SOC). Therefore, several impedance spectra (similar to
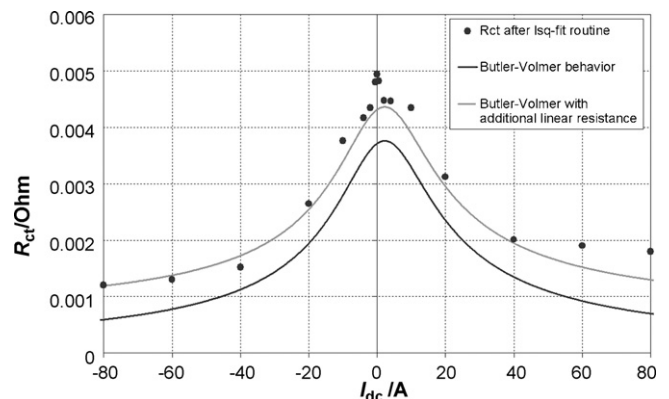

Fig. 3. Non-linear Butler–Volmer behavior (charge-transfer resistance) of a NiMH battery at 27 °C and 70% SOC (battery type: Sanyo Hr-DP, 6.5 Ah); black points: R_{ct} values determined by a least square fit routine, black curve: pure Butler–Volmer behavior ($n = 1$, $\alpha = 0.46$, $I_0 = 7$ A), grey curve: Butler–Volmer behavior with an additional linear resistance of 0.6 mΩ.
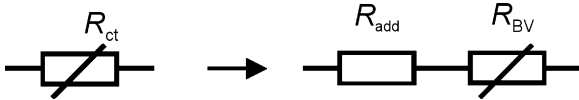
Fig. 4. Detailed representation of the non-linear resistor R_{ct} (cp. Fig. 2).

those shown in Fig. 1) have been evaluated with different super-imposed direct currents I_{dc} in a range from $-80\,A$ up to $+80\,A$ ($\sim\pm12C$ rate). The evaluation of R_{ct} has been carried out subsequently for each impedance measurement at different direct currents by using the equivalent circuit (Fig. 2) and a least square fit routine. The points correspond to the values that arise from this fitting procedure. A Butler–Volmer behavior is observable (black solid curve), however, a constant and current independent deviation has to be solved by adding an linear resistance. A microscopic physico-chemical explanation for the offset is unknown up to date and will be subject of further research efforts. However, the final result (grey curve) is absolutely satisfying for this kind of modeling and the later application of the NiMH model.

The resistor R_{ct} can finally be modeled by means of a series connection of a non-linear resistor R_{BV} (representing Eq. (1)) and a linear resistor R_{add} as presented in Fig. 4.

The remaining components of the electrical circuit (Fig. 2) have been parameterized by a least square fit routine as well. To enlarge the validity range to other temperatures and SOCs, the impedance spectra (with different I_{dc}) have to be measured at various temperatures and SOCs. The presented model has been parameterized for an array of temperatures (-18, 25 and $50\,°C$) and different states of charge (20, 40, 70 and 90%).

3. Hysteresis phenomenon in NiMH batteries

For most electrochemical systems the equilibrium potential is unambiguously defined by the state of charge. However, the nickel electrode shows a significant hysteresis of the open circuit potential, i.e. the potential does not depend solely on the state of charge but also on the history of charging and discharging of the electrode [6,8,9]. Systematic investigations on the nature of the equilibrium potential hysteresis of the nickel electrode by Podolske Ta et al. [9] and Srinivasan et al. [8] lead to the following characterization of the hysteresis, that could be corroborated by own measurements:

- The hysteresis is static, i.e. it remains after a charging or discharging current is switched off, even for a period of time that exceeds time constants of mass transport inside the electrodes significantly.
- The hysteresis is independent on the preceding current rate.
- The hysteresis is not only characterized by the boundary curves but also by intermediate sub-hysteresis loops.

These characteristics of the hysteresis are in accordance with a domain theory, that states that the electrode material is composed of clearly separated regions (domains) each of which exhibits two or more metastable states ([8,9]). The actual cause of the metastability is yet still a matter of scientific discussion.
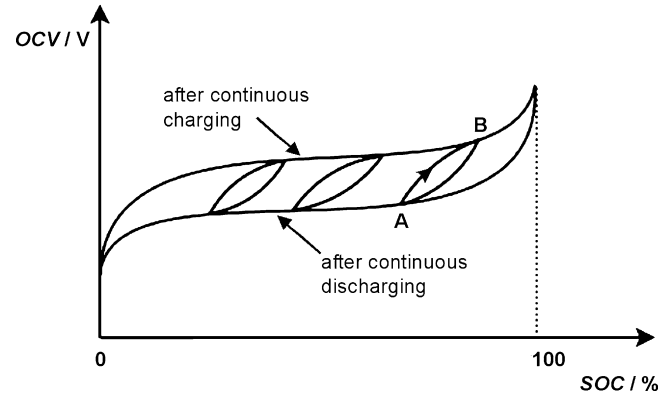

Fig. 5. Schematic presentation of the hysteresis phenomenon of NiMH batteries; equilibrium potential is not clearly determined by SOC but rather dependent on pre-treatment of the battery; battery voltage is depicted without current flow (measurement data can be found in Fig. 11, right hand).

One possible explanation is a change of the energy necessary for insertion or extraction of ions due to expansion and contraction of the intercalation material [9], another is a phase separation in the solid solution of $Ni(OH)_2$ and $NiOOH$ in the nickel electrode [8]. Experimental results on laboratory scale electrodes have shown that the composition of the electrodes – especially the insertion of cobalt – and the ageing of the electrodes affects the potential level but not the shape of the hysteresis loop ([8,9]). However, an electrochemical explanation of the equilibrium potential hysteresis is out of the scope of this paper; in the following a model will be developed that describes the effect quantitatively, can be parameterized by electrical measurements and is efficient with respect to computation time in a computer simulation model.

The lower and an upper-boundary equilibrium-potential curve measurable at open circuit conditions after charging or discharging periods is shown in Fig. 11 (measurements) and Fig. 5 (schematic illustration). Moreover, the intermediate range can be reached if the battery is operated with shallow cycles (depicted with small cycles). If the battery is for example continuously discharged until "A" and then re-charged, the equilibrium potential (measured *without* current flow) will follow the upper part of the small cycle ("A" to "B") and then finally describe the outer curve until 100% SOC. The necessity of an accurate modeling of this effect becomes obvious in Fig. 6 which illustrates that the hysteresis effect can be even more significant than the dynamic overvoltages up to absolute current rates of $|I_{batt}| \leq 20\,A$.

According to systematic investigations, the hysteresis effect depends exclusively on the charged or discharged amount of ampere hours. Comprehensive tests and conclusions showed that the current rate does not influence the equilibrium-potential level. A test with alternating discharging and charging pulses (different current rates but constant amounts of 3000 As) was carried out (Fig. 6). Rest periods of 1000 s duration were performed after each pulse to check the equilibrium potential. The gap between the straight lines (upper and lower equilibrium-potential curves) is not affected by the current rate which is in line with the findings in [6].
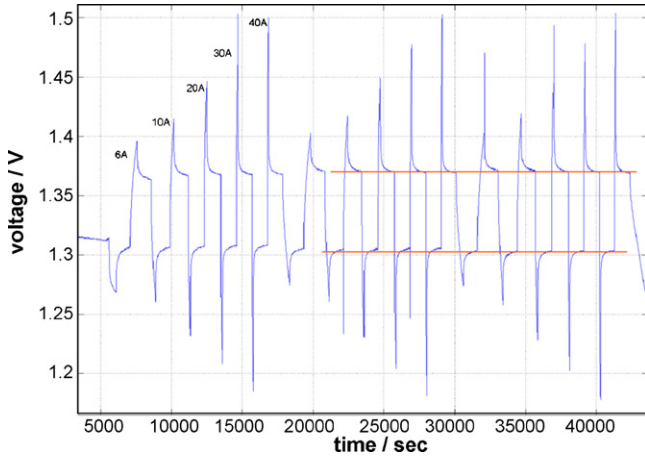
Fig. 6. Alternating charging and discharging pulses with different current rates but with a constant amount of 3000 As per pulse and rest periods of 1000 s in between; the hysteresis effect (gap between the straight lines) is independent of the current rate (battery type: Sanyo Hr-DP, 6.5 Ah/70% SOC, 27 °C).

3.1. Modeling of the hysteresis phenomenon

Generally, the equilibrium potential (U_0) of a battery cell can be modeled by a SOC-dependent voltage source. Since the NiMH equilibrium-potential behavior is seriously influenced by the above described phenomenon, the voltage source has to be adapted to a more complex model. The complete equivalent-circuit is depicted in Fig. 7, the detailed algorithm to calculate the equilibrium potential U_0(SOC, hyst) is addressed below.

U_0 is calculated by the sum of the lower SOC-dependent boundary voltage U_{LB} and an additional voltage U_{hyst} which considers the hysteresis effect of partial cycling (Eq. (2)). The maximum value of U_0 is limited by the upper boundary U_{UB}, the voltage U_{hyst} is limited SOC-dependently by the gap of the lower and upper boundary

$$U_0(\text{SOC}) = U_{LB}(\text{SOC}) + U_{hyst} \quad \text{with } U_0(\text{SOC}) \leq U_{UB}(\text{SOC})$$

(2)

Both, U_{LB}(SOC) and U_{UB}(SOC) can easily be modeled by a fixed polynomial approximation (5th order) with the SOC as the input value. The SOC is calculated according to Eq. (3) with I as the battery current and C_N as the nominal battery capacity (convention: charging $I > 0$/discharging $I < 0$). The gassing reaction can be taken into account by including the gassing current I_{gas} when integrating the battery current as shown in Eq. (3). The gassing current is a non-linear function of temperature and potential. A proposal for an appropriate modeling approach of
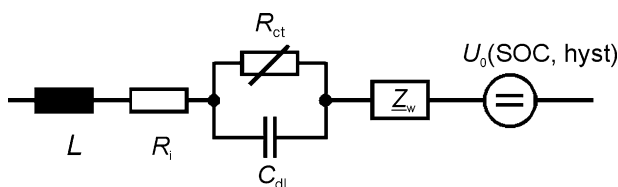

Fig. 7. Equivalent electrical circuit diagram of a NiMH battery considering the equilibrium potential which shows a hysteresis effect.
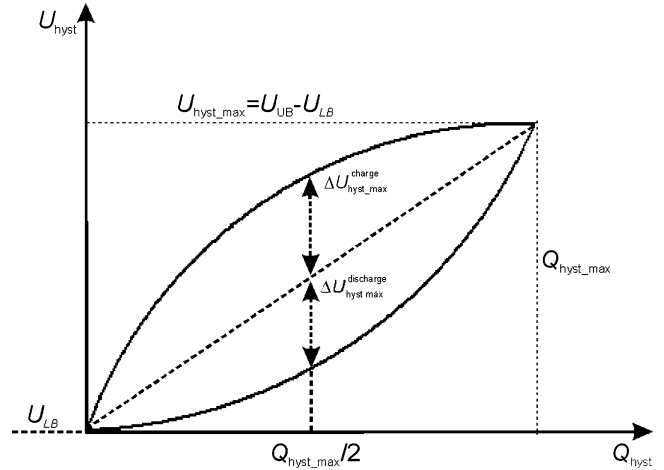

Fig. 8. Closer examination of the shape of the inner course of the equilibrium potential between the outer boundaries of the hysteresis curves (cp. Fig. 5).

the gassing reaction is given below and its necessity is discussed.

$$\text{SOC} = \text{SOC}(t = 0) + \left[\frac{\int_{t=0}^{t}(I - I_{gas})d\tau}{C_N} 100 \right]$$

with SOC $\leq$ 100%

(3)

U_{hys} has to be calculated during the simulation by a more complex algorithm. Therefore, a new parameter Q_{hyst} has to be defined (Eq. (4))

$$Q_{hyst} = \int I \, dt \quad \text{with } 0 \leq Q_{hyst} \leq Q_{hyst\_max}$$

(4)

Q_{hyst} sums up the charge-transfer current during a microcycle of the hysteresis effect. Q_{hyst} is equivalent to 0 when the battery only has been continuously discharged and the equilibrium potential follows the lower boundary (see Fig. 5). In case the battery is subjected to a microcycle (e.g. from "A" to "B", Fig. 5), Q_{hyst} increases and is finally limited at the value Q_{hyst_max} when the upper boundary is reached (at "B"). Q_{hyst_max} has to be determined by measurements (see Section 3.2). U_{hyst} is consequently equal to 0 V at $Q_{hyst} = 0$ As and $U_{hyst} = U_{UB}(\text{SOC}) - U_{LB}(\text{SOC}) = U_{hyst\_max}(\text{SOC})$ at $Q_{hyst} = Q_{hyst\_max}$. The maximum hysteresis voltage U_{hyst_max} has also to be deduced from measurements (see Section 3.2).

Considering these basic principles, only the shape of the course of the voltage during a shallow cycle between the outer boundaries has to be considered (Fig. 8). Therefore, the maximum stretching of the inner voltage characteristic $\Delta U_{hyst\_max}^{charge}$ for charging and $\Delta U_{hyst\_max}^{discharge}$ for discharging (at $Q_{hyst\_max}/2$) have to be evaluated by measurements (see Section 3.2). Since the hysteresis voltages at $Q_{hyst} = 0$, at $Q_{hyst} = Q_{hyst\_max}/2$ and $Q_{hyst} = Q_{hyst\_max}$ are thus determined, both curves can be approximated by polynomial equations of second order. By means of the limitations U_{hyst_max}(SOC) and U_{LB}(SOC), the stability of the hysteresis model over the complete SOC range is assured. Completely reasonable voltage values cannot be achieved since the lower and the upper boundaries cannot be overstepped.
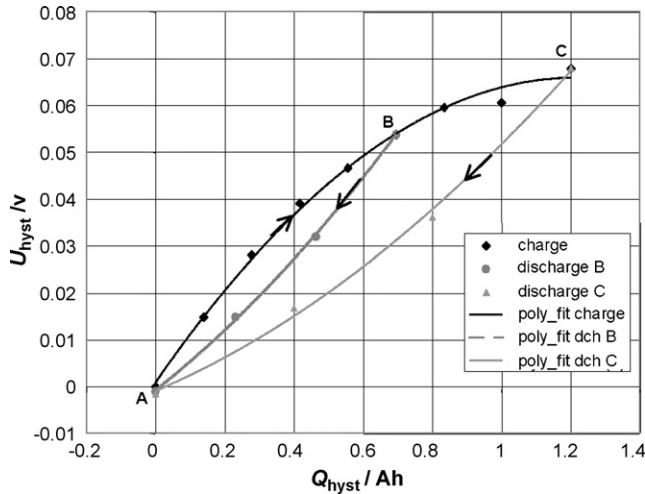
Fig. 9. Measurement of the inner voltage curves between lower and upper boundary, two different discharging periods (B: after 0.7 Ah charging, C: after 1.2 Ah charging) (battery type: Sanyo Hr-DP, 6.5 Ah/70% SOC, 27 °C).

Fig. 10. Exemplary illustration of the modeling of $U_{hsyt}(Q_{hyst})$ when the battery charge throughput is smaller than Q_{hyst_max}.

A more dynamic operation with smaller Ah throughputs than Q_{hyst_max} leads to processes inside the two already illustrated (Fig. 8) voltage curves. The measured data in Fig. 9 illustrate an appropriate test:

The battery has been continuously discharged to 70% SOC (which means Q_{hyst} equals 0 Ah). Subsequently, the battery has been charged with 10 A up to $Q_{hyst} = 0.7$ Ah (9.3% C_N, point "B" in the graph) and charged to $Q_{hyst} = 1.2$ Ah (18.5% C_N, point "C") respectively. Rest periods (1000 s) have been introduced to determine the equilibrium potential and U_{hyst} during the test. After reaching point B and C respectively, the battery has been discharged with −10 A until $Q_{hyst} = 0$ Ah again. A very similar symmetry of both curves ("A → B → A" and "A → C → A") can be observed considering a scaling factor which is linear to the actual amount of Q_{hyst}. This correlation can be used for modeling (Eqs. (5) and (6))

$$\Delta U_{hyst}^{discharge} = \Delta U_{hyst\_max}^{discharge} \frac{Q_{hyst}}{Q_{hyst\_max}} \quad (5)$$

$$\Delta U_{hyst}^{charge} = \Delta U_{hyst\_max}^{charge} \frac{Q_{hyst\_max} - Q_{hyst}}{Q_{hyst\_max}} \quad (6)$$

The outer voltage curves (Fig. 8) can be approximated by second order polynomials as mentioned. Using Eqs. (5) and (6), the same procedure can be applied when the Ah throughput is smaller than Q_{hyst_max}. To explain the employed algorithm, a charging/discharging sequence is explained by means of Fig. 10 (schematic, no measurement) as an example.

The sequence starts at point "A". Initially, the sign of the current is determined. Since the first pulse is a charging pulse, the voltage starts to rise according to the charging curve "'ACB". When charging is finished at some point (here: "C"), this point corresponds to the first point of the new discharging curve "CDA". The second point is the starting point "A". The third point ("D") can be determined by considering half of the charged value (charging from "A" to "C") and using Eq. (5). This is sufficient for the calculation of the polynomial coefficients for the discharging curve "CDA".

Instead of a finished discharging to point "A", the discharging may be finished in point "E" and charging starts again. The first point for the calculation of the next charging period is point "E", the second is again the saturation point B. For the calculation of the charging curves, point "B" is always relevant as the reference point, and for the calculation of the discharging curve point "A" is the reference point. The still needed third point for the coef-
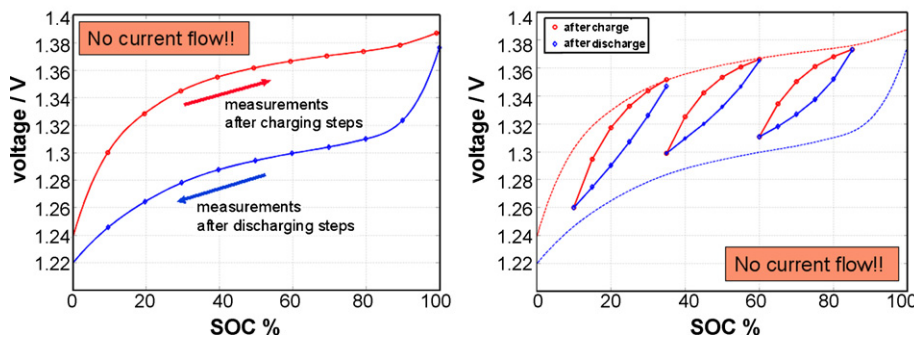

Fig. 11. (left hand) Measured equilibrium-potential values of a NiMH battery (points); lower curve measured after discharging steps (−10 A) with rest periods (1000 s) in between, upper curve after charging steps (+10 A); (right hand) Measurement data of the inner voltage curves according to the measurement procedure illustrated in Fig. 9 (battery type: Panasonic HHR 650D, 6.5 Ah/27 °C).
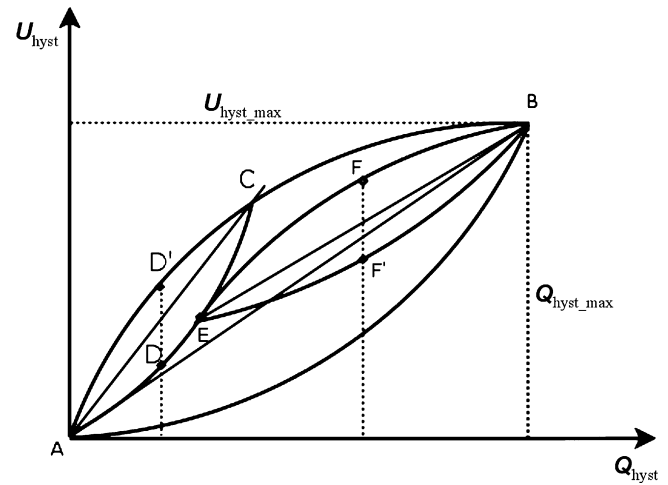
ficients of the new charging curve ("EFB") can be calculated again by using the similarity (Eq. (6)).

3.2. Parameterization of the hysteresis phenomenon

In the following paragraphs details are given on how to parameterize the model for the hysteresis.

3.2.1. Determination of $U_{LB}(SOC)$ and $U_{UB}(SOC)$

Measurement results to parameterize the lower and the upper boundary are illustrated in Fig. 11 (left hand). Therefore, a fully charged NiMH battery (nominal capacity 6.5 Ah) has been discharged stepwise with a current rate of $I = -10$ A. Again, rest periods of 1000 s after each discharging event (10% of C_N) have been made to measure the equilibrium-potential. Subsequently, the battery has been fully charged ($I = 10$ A) using the same procedure. For the SOC determination, coulombic losses due to gassing have been considered by means of the proposed gassing model (Section 4). For the implementation, the boundary curves are approximated by polynomials of fifth order.

3.2.2. Determination of Q_{hyst_max}, $\Delta U_{hyst\_max}^{charge}$ and $\Delta U_{hyst\_max}^{discharge}$

The procedure according to Fig. 9 has been applied at three different SOC values (initiated at 35, 60, and 80% SOC). Measurement data can be found in Fig. 11 (right hand). The deviations between the lowest points of the inner curves and the lower boundary curve ($U_{LB}(SOC)$) are addressed in the discussion part. Saturation values of $Q_{hyst\_max} \approx 0.8\ldots1.2$ Ah have been found. The maximum stretching of the inner voltage curves has been $\Delta U_{hyst\_max}^{charge} \approx 17\ldots20$ mV and $\Delta U_{hyst\_max}^{discharge} \approx 5\ldots10$ mV. The stretching during charging was always significantly higher than in case of discharging. The values have been determined for cylindrical NiMH batteries with $C_N = 6.5$ Ah (samples from Sanyo and Panasonic).

3.2.3. Determination of U_{hyst_max}

The maximum hysteresis voltage $U_{hyst\_max}(SOC)$ corresponds to the difference of $U_{UB}(SOC)$ and $U_{LB}(SOC)$. Values of up to 70 mV have been found

$$U_{hyst\_max}(SOC) = U_{UB}(SOC) - U_{LB}(SOC). \tag{7}$$

4. Proposal of a gassing model

Measurements were performed at different battery temperatures to evaluate the gassing characteristic. Therefore, a fully charged cell was overcharged with different constant currents in a range of 0.325 A (0.1 C) up to 3.25 A (1 C). The corresponding cell voltage was collected after its stabilization. Fig. 12 gives the measurement data by using a semi-logarithmic illustration.

The lines represent the results of Eq. (8) which can be used as an additional model part. T corresponds to the battery temperature and U to the battery voltage, however without the ohmic overpotential which does not affect electrolyte decomposition. U_0 corresponds to the decomposition voltage of water with
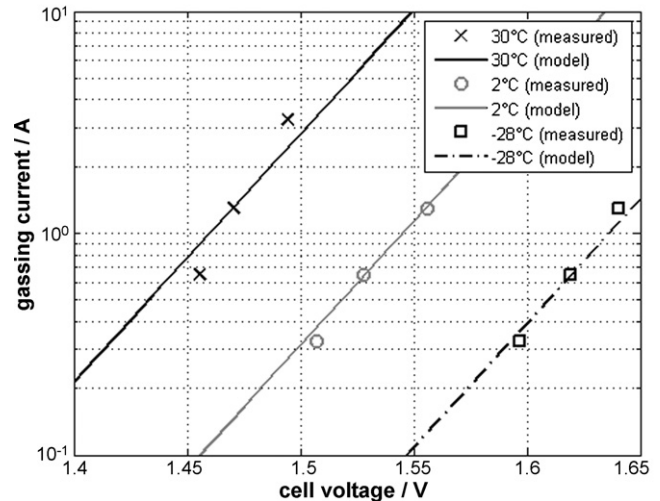

Fig. 12. Gassing currents at 30 °C, 2 °C and −28 °C and different cell voltages; the temperature of the battery could be regulated to a range of ±2 °C around the illustrated values; the lines represent the results of the proposed gassing model.

1.23 V. The remaining parameters are freely chosen values; the values listed in Table 1 result an accurate match of the measured data (see Fig. 12)

$$I_{gas} = I_0 \exp(\alpha(U - U_0))\exp(\beta(T - T_0)) \tag{8}$$

The necessity of this modeling part depends on the application of the model. If the voltage behavior has to be investigated for quite short periods, the gassing model can be neglected probably. This is exemplarily demonstrated by Fig. 13. The left hand figure illustrates the simulated voltage responses to a profile with alternating current steps (±30 A, ∼4.6 C) at 27 °C and 70% SOC. Rest periods are inserted between the charging and discharging steps. The duration of each step and the rest periods amount to 30 s. The simulations have been performed with and without gassing model. Even after a period of half an hour, no voltage deviations can be observed between both approaches.

However, the gassing influences cannot be neglected if the simulation of the battery efficiency is aimed. This is illustrated exemplarily by means of the right hand figure. The charging current is reduced by the coulombic losses (gassing current) which lead to a clearly decreasing state of charge (∼1.5% SOC during this test). This effect intensifies with more intensive charging cycles, with increased SOC and with increased temperature. However, since the description of the pure voltage behavior is the main focus of this paper, the gassing influences were not considered for the simulated (quite short) voltage courses given in Section 5 ($I_{gas} = 0$).

Table 1
Parameters for modeling of the gassing behavior by means of Eq. (8) corresponding to measurement data illustrated in Fig. 12

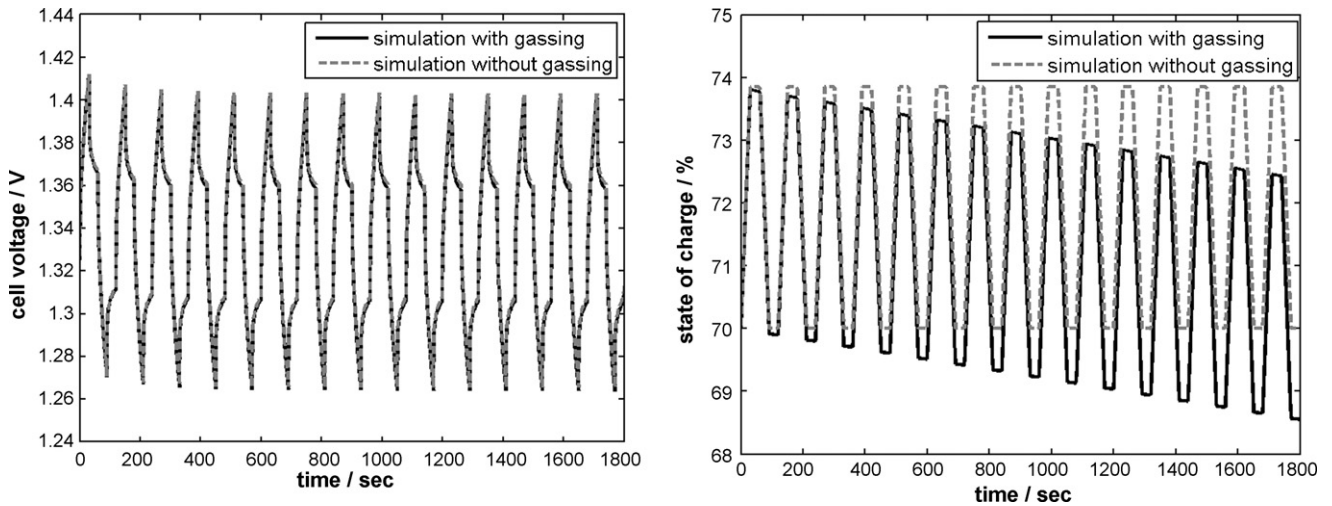|	
I_0	1.808 mA
T_0	25 °C
α	25.74 V^{-1}
β	0.078 °C^{-1}

Fig. 13. Simulation with and without gassing model of alternating current steps at 27 °C with 30 s duration, ±30 A battery current and rest periods in between; the gassing influences on the voltage behavior are almost negligible for the simulated period of 0.5 h (left hand), the influences on the SOC calculation are not negligible (right hand).

5. Model evaluation

Comparisons among measured and simulated voltage curves over time are presented in this section. Step profiles with different dynamics (respectively step duration) and a wide range of current rates were applied to a battery (Sanyo Hr-DP, 6.5 Ah). Fig. 14 exemplarily illustrates the procedure of the current steps (left hand) and the corresponding cell voltage (right hand). It has to be noted that the cell voltage changes even though no current is applied. The recovering voltage is caused by the double layer capacitance C_{dl} and the diffusion processes of the charge carriers (see Section 2). Figs. 15–17 illustrate the simulation and measurement results according to this kind of input profile.

Fig. 15 gives the results for the steps with 10 s duration. The test was carried out at 27 °C and 20% SOC. The current range amounted to 0.5 to 15 times the C-rate.

A further illustration compares measured and simulated data by using shorter steps of 1 s duration each. This test was performed at 50 °C and 20% SOC. The current range corresponds to the current range which was the basis for the data in Fig. 15 as well.

Fig. 17 depicts a comparison for input currents in a range from 0.5 to 4.6 times the C-rate at 27 °C and 70% SOC. Alternating current pulses with a lower dynamic of 100 s duration were applied.

Finally, a current profile is illustrated that forces the hysteresis effect and illustrates the advantages of the actual hysteresis model. Therefore, current pulses with 10 A were applied, however with different duration and therefore different amounts of charge. The current profile is given in (Fig. 18). The cumulative amount of charge of the three consecutively repeated discharge pulses corresponds to the amount of Ah of the preceding charging step. Moreover, the total amount of charged Ah was increased subsequently. Hence, hysteresis curves of different sizes (cp. Fig. 9) have to be simulated accurately to match the measured voltage (Fig. 19).
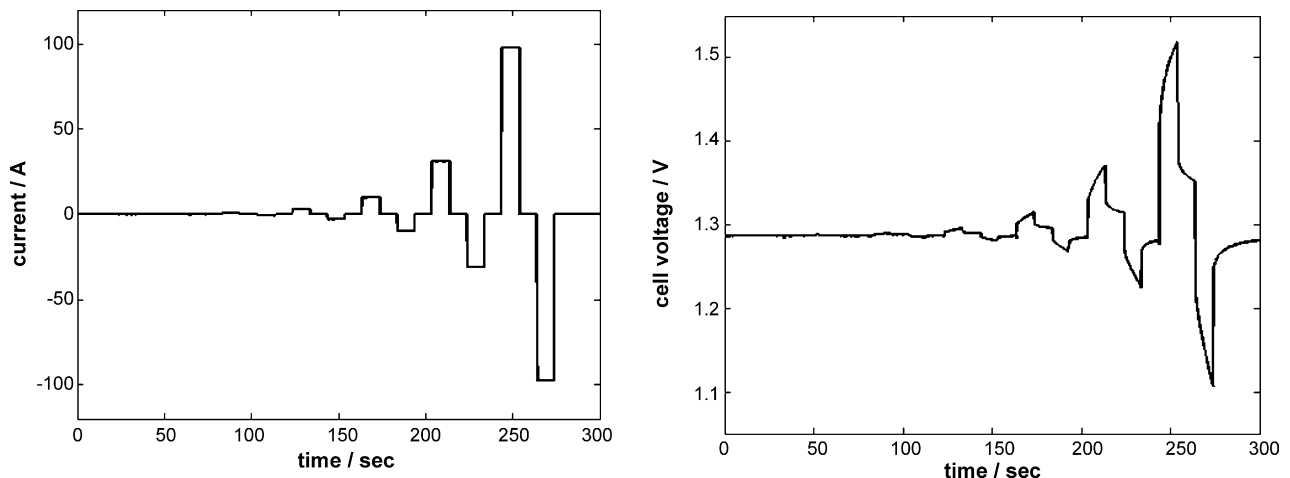

Fig. 14. Exemplary illustration of input current steps used for model evaluation; repetitions of these current steps have been applied to a real battery and to the model with different step durations; results are depicted subsequently.
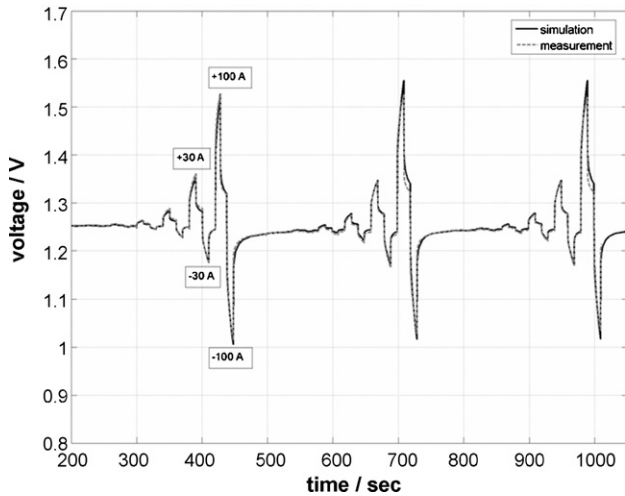
Fig. 15. Comparison of measured and simulated battery voltage corresponding to an alternating profile with absolute battery-currents of up to 100 A at 20% SOC and 27 °C (battery type: Sanyo Hr-DP, 6.5 Ah).

Fig. 18. Input current profile to force the hysteresis effect, the discharged amount of each discharge triple corresponds to the preceding charging step.
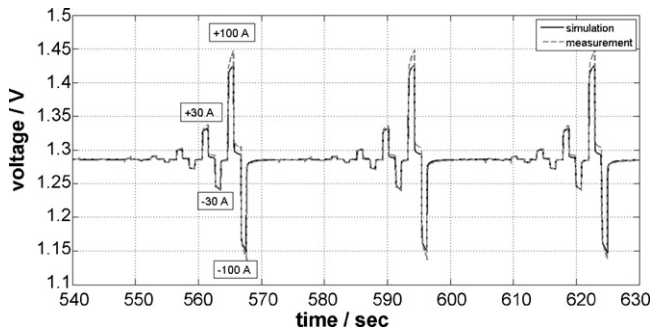

Fig. 16. Comparison of measured and simulated battery voltage corresponding to an alternating step profile with absolute battery currents of up to 100 A at 20% SOC and 50 °C (battery type: Sanyo Hr-DP, 6.5 Ah).

6. Discussion

An accurate agreement between the simulated and the measured battery behavior has been demonstrated. These results have been achieved by combining an impedance-based model core which describes the battery dynamic in a wide range and a hysteresis model that successfully describes the hysteresis of the equilibrium-potential of NiMH batteries. However, the hysteresis model is a purely phenomenological approach and a certain error between the modeling assumption and the measurement data becomes obvious. For modeling, small inner curves with connecting points to the outer hysteresis curve have been assumed (cp. Fig. 5 (schematic)). This approach has been accepted even though measurements indicate a voltage error of approximately 10 mV where the inner curves do not really join the lower boundary curve (cp. Fig. 11 (measurement)). More theoretical explanation for the hysteresis phenomenon would be beneficial for the understanding and model implementation. The hysteresis phenomenon of NiMH batteries has been previously investigated and explained on a qualitative basis (e.g. in [6,8,9]), but no consistent model has been presented that explains the effect quantitatively.
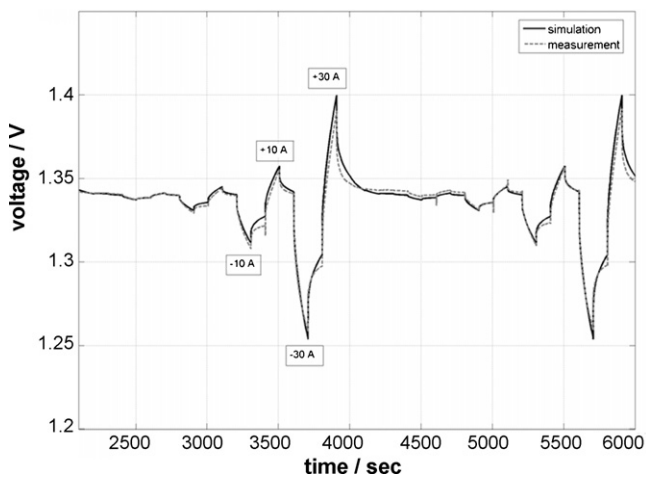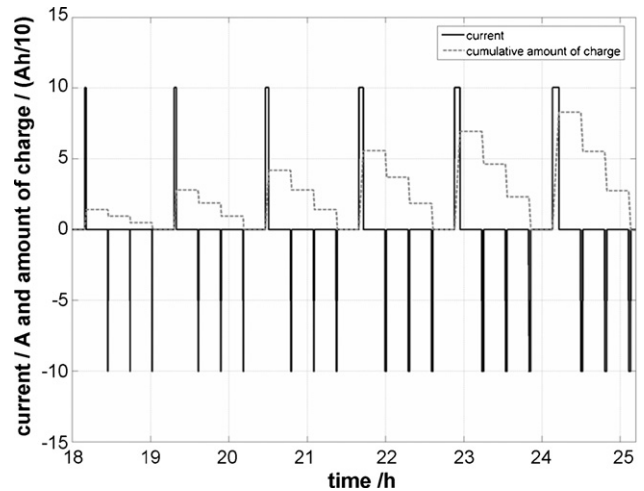

Fig. 17. Comparison of measured and simulated battery voltage corresponding to an alternating profile with absolute battery currents up to 30 A at 70% SOC and 27 °C (battery type: Sanyo Hr-DP, 6.5 Ah).
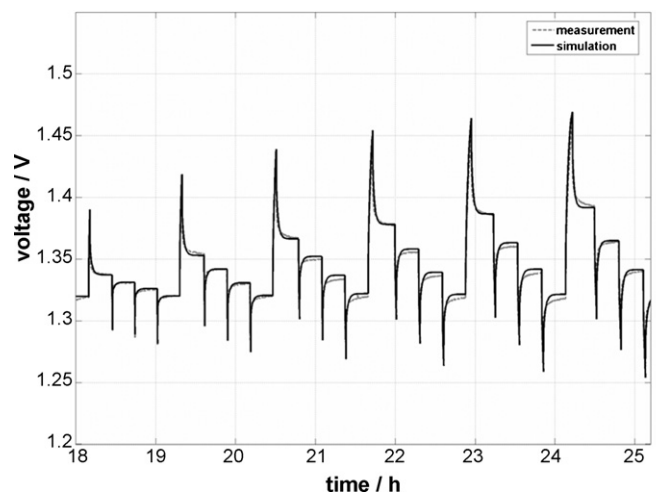

Fig. 19. Voltage response to the current profile which is depicted in Fig. 18 at 27 °C and 70% SOC (battery type: Sanyo Hr-DP, 6.5 Ah).

Measurements have been shown for 27 °C and 50 °C within this paper. The impedance based modeling approach has been proven down to −18 °C as well. However, the collection of impedance data at deep temperatures is more difficult (the model parameterization, respectively). On the one hand, the battery heats up quite fast during tests with bias current. On the other hand, the transport of charge carriers becomes more relevant with decreased battery temperature. Investigations on transport processes however demand quite high Ah throughputs which violate the rules of impedance spectroscopy. "Quasi-steady" conditions with no significant changes of the SOC have to be kept during the measurement. Consequently, the purely impedance modeling approach is restricted. An enlargement of the model's validity range (including large Ah-throughputs combined with deep temperatures) could be achieved by additional model parts such as a separated transport model which demands no impedance measurements. This has been applied for the modeling of lead-acid batteries already [10].

Furthermore, the battery model has to be equipped by an appropriate gassing model if the simulation of the battery efficiency is focused (not only the voltage behavior for a short duration). A possible gassing model has been proposed which can be connected in parallel to the RC-element, the Warburg impedance and the equilibrium-potential calculation (Fig. 7). This approach has been employed successfully as well for lead-acid battery models [11].

7. Summary

An impedance-based modeling approach, that copes with the specific battery characteristics and offers the development and parameterization of powerful models covering a wide dynamic range, has been applied to NiMH battery technology. This modeling approach has been successfully applied to further bat-tery technologies such as Li-ion, lead-acid and electrochemical double-layer capacitors [4]. Besides the impedance-based core of the model, the typical hysteresis in the equilibrium voltage, which is very pronounced for NiMH batteries has been described in detail and an appropriate modeling approach has been introduced. Finally, the NiMH battery model has been evaluated with comparisons among measured and simulated voltage data in the time domain by using input current profiles at different states of charge, with significantly different current rates and various time constants (Section 5). Limits and valuable upgrades of the NiMH battery model have been finally discussed. The proposed gassing model has to be considered if the simulation of the battery efficiency is focused.

References

[1] J.R. Macdonald (Ed.), Impedance Spectroscopy, Emphasizing Solid Materials and Systems, John Wiley & Sons, 1987, ISBN 0-471-83122-0.
[2] H. Blanke, M. Kiel, T. Sanders, T. Baumhöfer, B. Fricke, D.U. Sauer, Tech. Mitt. 99 (1/2) (2006) 231–234.
[3] S. Buller, M. Thele, E. Karden, R.W. De, Doncker, J. Power Sources 113 (2003) 422–430.
[4] S. Buller, Impedance-based simulation models for energy storage devices in advanced automotive power systems, PhD Thesis, RWTH Aachen University, 2002, ISBN: 3-8322-1225-6.
[5] E. Kuhn, C. Forgez, P. Lagonotte, G. Friedrich, J. Power Sources 158 (2006) 1490–1497.
[6] M. Verbrugge, E. Tate, J. Power Sources 126 (2004) 236–249.
[7] K. Bundy, M. Karlsson, G. Lindbergh, A. Lundqvist, J. Power Sources 72 (1998) 118–125.
[8] V. Srinivasan, J.W. Weidner, J. Newman, J. Electrochem. Soc. 148 (2001) 969–980.
[9] K. Podolske Ta, J. Newman, J. Electrochem. Soc. 146 (1999) 2769–2779.
[10] M. Thele, S. Buller, D.U. Sauer, R.W. De Doncker, E. Karden, J. Power Sources 144 (2005) 461–466.
[11] M. Thele, E. Karden, E. Surewaard, D.U. Sauer, J. Power Sources 158 (2006) 953–963.